

Unusual Crystallization Behavior of Organoclay Reinforced Poly(L-lactic acid) Nanocomposites

Vahik Krikorian and Darrin J. Pochan*

Department of Materials Science and Engineering and Delaware Biotechnology Institute, University of Delaware, Newark, Delaware 19716

Received April 13, 2004; Revised Manuscript Received June 9, 2004

ABSTRACT: The effect of organically modified montmorillonite clay addition on crystallization of a polymer matrix has been studied. Two types of commercially available organoclays with different extent of miscibility with a polymer matrix were employed, leading to fully exfoliated (high miscibility) and intercalated (low miscibility) nanocomposite morphologies. The nanocomposites were fabricated via the exfoliation-adsorption technique with the biodegradable polyester matrix polymer poly(L-lactic acid) (PLLA). As-cast nanocomposite films were melted and isothermally crystallized at different temperatures. Bulk kinetics studies and radial spherulite growth rates indicate that when a high degree of filler-polymer matrix miscibility is present, nucleation properties of the organoclay are low relative to the less miscible organoclay. Therefore, the overall bulk crystallization rate was increased in the intercalated system and somewhat retarded in the exfoliated system. Surprisingly, spherulite growth rates were significantly increased relative to the bulk in the fully exfoliated nanocomposite. This phenomenon, linked with less effective nucleation properties, resulted in significantly bigger spherulite sizes in the exfoliated nanocomposite. The overall percent of crystallinity and the size of crystalline domains decreased by addition of organoclays and are the lowest in the fully exfoliated case.

1. Introduction

The idea of adding inorganic fillers to organic matrices with the aim of improving desired matrix properties has deep roots in the history of macromolecules. One can categorize these fillers on the basis of their physical dimensions; typically, if at least one dimension of the filler is in the nanometer range, the resulting composite is called a nanocomposite. One class of polymer-based nanocomposites is the polymer layered-silicate nanocomposite (PLSN), which has attracted significant academic and industrial interest in the past decade. In this class of hybrid materials the reinforcement phase can consist of natural or synthetic clay, both of which are composed of regular stacking of silicate layers bound together with weak interatomic forces. Depending on physical properties of the polymer, clay, and/or processing conditions three morphologies, exclusively or in combination, can be achieved: a microphase-separated conventional composite, an intercalated nanocomposite, or an exfoliated nanocomposite.¹ The critical role of polymer matrix crystal nucleation rate, crystallization rate, and ultimate crystalline morphology on the final physical properties of filled polymer composites make nanocomposites crystallization studies vital from both industrial and academic perspectives.

Since 1987 when Toyota researchers first developed nylon-6/montmorillonite nanocomposites,^{2,3} many studies have shown that incorporation of high aspect ratio inorganic phases to polymeric matrices often leads to dramatic improvements in material properties such as better mechanical properties,¹ better barrier properties,⁴ reduced flammability,⁵ and higher heat distortion temperatures.⁶ These improved properties are achievable at very low clay loadings, considerably lower than what is required for conventional fillers such as glass bead/fiber, talc, or carbon black/graphite.

Regardless of filler dimensionality, incorporation of a reinforcement phase can affect the crystallization kinetics, crystallite size, crystalline morphology, and degree of crystallinity of the matrix. For example, in the case of carbon black filled⁷ or glass bead filled composites,^{8,9} it has been shown that by going toward smaller particle size more reinforcement phase surface area is created at a given filler volume fraction, resulting in more enhanced filler/matrix interactions and consequent dramatic effects on the crystallization properties of the polymeric matrices. Polymer crystallization behavior in the presence of inorganics has been the topic of extensive studies;¹⁰ most of the work has focused on bulk crystallization while only a few investigations have reported the effect of fillers on radial spherulite growth rates. All inorganically reinforced polymers exhibit increased bulk crystallization kinetics relative to the neat polymer. This phenomenon is uniformly attributed to higher heterogeneous nucleation rates, demonstrated by increases in determined Avrami exponents. In contrast, linear spherulitic growth rates have been observed to vary greatly in inorganic reinforced polymers relative to the neat polymer. For example, St Pierre et al.^{11–14} studied silica particle filled isotactic poly(propylene oxide) and isotactic polystyrene systems. They found that even at very low silica loadings, as low as 0.1 vol %, the filler acted as a nucleation agent, thus greatly enhancing the bulk crystallization rate but also significantly retarding the spherulite growth rate. This trend was ascribed to the adsorption of the polymer chains onto the filler surfaces, which increased the viscosity and, consequently, decreased the transport of crystallizable segments to the crystal growth front. In contrast, Burke et al.¹⁵ observed enhancements in bulk crystallization kinetics but no change in polypropylene spherulitic growth rate filled with TiO₂ even though similarly enhanced nucleation properties were observed. Similar results were observed by Raimo et al.¹⁶ in which

* Corresponding author. E-mail: Pochan@udel.edu.

addition of TiO₂ particles to ethylene-propylene (EP) copolymer acted to nucleate crystallization. At higher crystallization temperatures the radial spherulite growth rate was unchanged while, surprisingly, at lower crystallization temperatures the spherulite growth rate was higher than that of neat copolymer. Wang et al.¹⁷ have shown that by varying the interfacial properties of BaSO₄ filler with different chemical modifiers they could alter the polypropylene/BaSO₄ interfacial interaction and the polypropylene spherulite growth rates. Addition of weakly interacting filler decreased the spherulite growth rate while the strongly interacting PP/BaSO₄ system displayed an even slower rate purportedly due to polymer chain confinement effects introduced by the attractive interaction at the filler/polymer interface. These widely varying observed effects of reinforcement on polymer spherulite growth inspire further studies described herein.

Another crystallization effect of polymer reinforcement, in both nanocomposites and conventional microscale filler composites, is that the filler can promote the growth of a specific crystalline form that is not favorable in the neat polymer. For instance, in the case of microscale fiber reinforced semicrystalline composites, under appropriate conditions, a highly oriented, so-called "transcrystalline layer"^{18,19} is formed on the fiber due to its high nucleating ability. It has been shown that in the case of nylon-6/clay nanocomposites the incorporation of clay promotes the growth of the γ -form⁶ of the nylon, while neat polymer tends to crystallize in α -form.²⁰ Similar changes in crystal formation were also observed in syndiotactic polystyrene (s-PS) in which the addition of clay promoted the generation of β -form crystals instead of the α -form.²¹⁻²³ Solid-state NMR studies of VanderHart et al.^{24,25} showed that nylon-6 γ -crystallites are formed in the proximity of the nylon-6/clay interface, and this phase is enhanced regardless of the nanocomposite formation technique. These results are in good agreement with Lincoln et al.,²⁶ who observed that γ -form crystals present in nylon-6/clay nanocomposites are very stable throughout a wide temperature range, perhaps explaining the high heat distortion temperatures observed. In addition, Liu et al. showed that in nonisothermal crystallization studies, in contrast to neat nylon-6, the degree of nanocomposite crystallinity surprisingly increases by increasing the cooling rate. This was in agreement with X-ray diffraction results and was attributed to the favored formation of the γ crystalline form at higher cooling rates.

The study of polymer matrix crystallization in clay nanocomposites is complicated by the extent of miscibility between the clay reinforcement and polymer matrix and, thus, the extent of intercalation vs exfoliation of the reinforcement phase. Differences in filler/polymer miscibility and filler dispersion can have significant effects on spherulite nucleation rates, bulk crystallization kinetics, and crystal morphology. Fornes et al. have shown that bulk polymer crystallization kinetics can be significantly increased at very low clay contents while higher clay loadings retard the overall bulk crystallization process.²⁷ Moreover, it has been shown that higher crystallization rates can be achieved in high molecular weight nylon-6 due to its greater extent of exfoliation.²⁷ The predominantly heterogeneous nucleation behavior displayed by clay in most currently studied polymer clay nanocomposites has made the study of spherulitic growth kinetics and morphology studies impractical

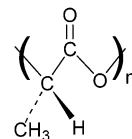


Figure 1. Chemical structure of poly(L-lactic acid) (PLLA).

with only a few contributions²⁸⁻³⁰ dedicated solely to the morphology of the spherulites. Somwangthanaroj et al.²⁹ studied the crystallization of PP-based layered silicate nanocomposites under quiescent and shear flow conditions. Higher crystallization rates were achieved in the case of intercalated nanocomposites. It was concluded that local stress and orientation of the matrix induced by shear alignment of clay may play a critical role in crystallization rate enhancement. In a similar system where maleic anhydride modified PP was used, even though intercalated clay acted as a nucleating agent, the linear spherulitic growth rate probed by light scattering was not influenced in the nanocomposites.²⁸ Similarly, Nam et al. observed increased nucleation but essentially no influence on spherulite growth rate in PLA/C₁₈-MMT nanocomposites (a slight increase in growth rate of the nanocomposite was attributed to molecular weight effects).³¹ In another study Hambir et al.³² reported fibrous crystallite formation in PP-based clay nanocomposites crystallized at higher temperatures. Intriguing results have been observed in the poly(ethylene oxide)/Na⁺-montmorillonite intercalated system.³⁰ This system is unique in that inorganic fillers enhance the crystallization of PEO while alkali cations such as Na⁺ hinder its crystallization. In this particular system spherulites growing from the melt in the presence of clay are not purely spherulitic but have jagged edges. While clay hinders the PEO crystallization, at small clay loadings the overall extent of crystallinity is not affected. However, the bulk crystallization rate becomes faster with the addition of clay due to enhanced nucleation. To explain this phenomenon, authors have proposed that primary nucleation takes place in the bulk, not on the intercalated clay platelets, and the spherulites grow normally until they encounter a clay platelet surrounded by amorphous regions. This is in contrast with the nylon-6 nanocomposites case³³ where it is proposed that during crystallization one molecular layer is nucleated on the clay platelet surface, thus preparing the surface for hydrogen bonding of the subsequent molecules, resulting in a lamellar pseudohexagonally packed structure on both sides of the clay.

Such disparate results in spherulite growth mechanisms and morphologies in semicrystalline polymer nanocomposites inspired this contribution. In the present study, the isothermal crystallization behavior of neat PLLA (Figure 1) and PLLA filled with 10 and 15 wt % organically modified clay have been studied. To investigate the effect of intercalated vs fully exfoliated nanocomposite morphologies within the same system, two types of commercially available organoclays, Cloisite 15A and 30B, were employed. In our previous work we found that the extent of miscibility between Cloisite 15A and 30B and PLLA dictated the extent of dispersion in the final nanocomposites—the more miscible organoclay, PLLA30B, led to completely exfoliated nanocomposites while the less miscible, PLLA15A, led to intercalated nanocomposites.³⁴ Conventional polarized light microscopy, atomic force microscopy (AFM), and differential scanning calorimetry (DSC) techniques were employed

to investigate the radial spherulite growth rate, spherulite morphology, and bulk crystallization kinetics, respectively. To qualitatively/macrospectively observe the distribution of silicate layers, energy-dispersive X-ray spectroscopy (EDS) was also used to monitor clay segregation after crystallization. Spherulitic growth rates and bulk crystallization kinetics are analyzed utilizing secondary nucleation theory and Avrami analysis. The overall degree of crystallinity, crystallization half-time, Avrami exponents, and crystallization induction time were obtained. We have found that the addition of a highly miscible organoclay into the matrix results in a lower degree of crystallinity, lower bulk crystallization rates, and much higher radial spherulitic growth rate compared to matrix reinforced by less miscible organoclay.

2. Theory

2.1. Spherulite Growth Rate. During polymer crystallization the growth face undergoes two different but related processes. One is the deposition of secondary nuclei on the growth face, and the other process is subsequent growth along the face at the sites where the secondary nuclei were formed. So there are two competing rates involved in this process that determine the regime in which the polymer crystallizes. On the basis of the secondary nuclei formation rate, i , and the lateral growth rate, g , the crystallization regimes can be defined as follows:³⁵

$$\begin{aligned} i \ll g & \quad \text{regime I} \\ i \sim g & \quad \text{regime II} \\ i > g & \quad \text{regime III} \end{aligned}$$

The temperature dependence of the growth rate of a linear polymer crystal, which undergoes chain folding, can be predicted by the secondary nucleation theory of polymer crystal growth³⁵⁻³⁷

$$G(T) = G_0 \exp\left(-\frac{U^*}{R(T_c - T_\infty)}\right) \exp\left(-\frac{K_g}{T_c \Delta T f}\right) \quad (\text{i})$$

where K_g is the nucleation/empirical constant defined as $K_g = nb\sigma\sigma_e T_m^2 / \Delta h_f k$ in which n is 4 for regimes I and III and 2 for regime II; b is the layer thickness; σ is the lateral surface energy; σ_e is the fold surface free energy; Δh_f is the heat of fusion per unit volume; k is the Boltzmann constant; T_c is the crystallization temperature; T_∞ is a temperature approximately 30 °C below the glass transition temperature (T_g), where it can be assumed that all the motions associated with the viscous flow are negligible; T_m is the equilibrium melting temperature; ΔT is the undercooling or $T_m - T_c$; U^* is the activation energy for transport of polymer segments to the growth front; R is the gas constant; and f is defined as $f = 2T_c / (T_c + T_m)$ to correct the changes in Δh_f at high undercoolings. The logarithm of eq i suggests that the plot of $\log G(T) + U^*/[2.303R(T_c - T_\infty)]$ vs $1/(T_c \Delta T)$ should be a straight line or, in the case of existence of different regimes, it should be a combination of straight lines with different slopes, i.e., different K_g 's.

According to the Hoffman and Weeks³⁸ expression, $T_m = T_m(1 - 1/2\beta) + T_c/2\beta$, where T_m is the melting point and β is a constant related to the edge free surface energy; T_m can be predicted by straight line extrapolation

of T_m vs T_c empirical plot to the point where T_m is equal to T_c .

2.2. Bulk Crystallization Kinetics. To describe the isothermal crystallization kinetics of neat PLLA and corresponding nanocomposites, the classical Avrami equation can be used:³⁹⁻⁴¹

$$1 - X_t = \exp(-Kt^n) \quad (\text{ii})$$

where X_t is the amount of crystallized material or the conversion degree to crystalline phase, n is the Avrami exponent, and K is an Avrami parameter depending on the geometry of the growing crystalline phase. In this model it is assumed that the material reaches 100% crystallinity.

During the isothermal crystallization, heat flow (dH/dt) can be probed over crystallization time via differential scanning calorimetry. One can derive the percent of ultimate crystallization vs time by using eq iii and applying it to the exothermic crystallization peak:

$$X_t = \frac{\int_0^t (dH/dt) dt}{\int_0^\infty (dH/dt) dt} \quad (\text{iii})$$

In this equation, the numerator is the crystallization heat generated up to time t and the denominator is the total heat produced by the completion of the entire crystallization process.

Taking the double logarithm of eq ii gives

$$\log(-\ln(1 - X_t)) = n \log K + n \log t \quad (\text{iv})$$

which suggests that $\log(-\ln(1 - X_t))$ vs $\log t$ should be linear, and K and n can be calculated by fitting a line to the experimental data. The Avrami exponent, n , is equal to the growth dimensionality plus one, and K is a function of growth geometry.

3. Experimental Section

3.1. Materials. Poly(L-lactic acid) (PLLA) was purchased from Polysciences Inc., Warrington, PA, with a viscosity molecular weight of 325 000–460 000 g/mol as reported by the manufacturer. As-received PLLA was purified by dissolution in chloroform and subsequent precipitation with methanol. Refined polymer was then dried in vacuo for 2 days at 80 °C and kept in desiccation until later use. Two types of organically modified MMT, Cloisite 30B and 15A, were purchased from Southern Clay Product Inc., Gonzales, TX, and used as received. These organoclays are prepared by modification of natural montmorillonite clays with different quaternary ammonium salts. The extent of cationic exchange and the chemical structure of the specific organic modifier of each of the organoclays are listed in Table 1 according to the data provided by the supplier.

Nanocomposite Preparation. Nanocomposites were prepared by using the solution-intercalation film-casting technique. For each final nanocomposite composition 100 mg of PLLA was dissolved in 10 mL of dichloromethane. Clay dispersions (<0.1 wt %) were obtained by suspension of well-dried clay in a separate beaker of dichloromethane. Calculations for varying final composite compositions were based on the inorganic component of the modified clay, thereby excluding the amount of organic modifier. (The inorganic amount in each of the organoclays was obtained by analysis of 10 mg of modified clay via thermal gravimetric analysis under dried air flow at 900 °C.) Both the PLLA solution and clay suspension were sonicated separately for 30 min with a Misonix 3000 probe sonicator at 21 W and room temperature (pulse mode was used to prevent from an extensive increase in tempera-

Table 1. Characteristics of Organoclays^a

| Clay Type | Extent of Modification [meq/100g clay] | Chemical Structure of Organic Modifier |
|--------------|---|---|
| Cloisite 30B | 90 | $\begin{array}{c} \text{CH}_2\text{CH}_2\text{OH} \\ \\ \text{H}_3\text{C}-\text{N}^+-\text{T} \\ \\ \text{CH}_2\text{CH}_2\text{OH} \end{array}$ |
| Cloisite 15A | 125 | $\begin{array}{c} \text{CH}_3 \\ \\ \text{H}_3\text{C}-\text{N}^+-\text{HT} \\ \\ \text{HT} \end{array}$ |

^a HT is hydrogenated tallow (~65% C18; ~30% C16; ~5% C14).

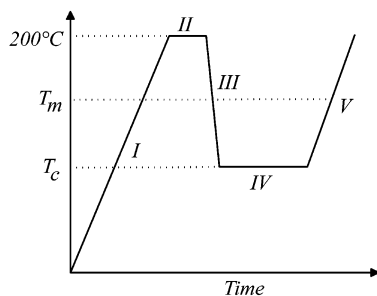


Figure 2. DSC heating cycles applied to as-cast films; T_c is the crystallization temperature, and T_m is the melting point.

ture) and subsequently mixed. The final mixture was further sonicated for 30 min. The mixture was then cast on a glass surface and kept in a desiccator for controlled evaporation of the solvent over 2 days. Eventually, optically clear nanocomposite films with thickness ranging from 500 to 700 μm were obtained and subsequently dried at 80 $^\circ\text{C}$ under vacuum for 2 days. All the samples for crystallization studies were cut from these films.

3.2. Thermal Analysis. Isothermal crystallization studies were performed on a TA-Instruments differential scanning calorimeter (DSC) model Q100 series instrument under constant nitrogen flow. The DSC samples were weighed such that all of the samples had identical PLLA content. The sample weight was maintained at low levels (1–2 mg) for all measurements in order to minimize any possible thermal lag during the scans. Each reported result is an average of five separate measurements. Temperature and heat of fusion were calibrated with an indium standard, and background subtraction was done according to TA Instruments protocols.

A schematic of all the isothermal crystallization runs is shown in Figure 2. As-cast samples were heated from room temperature to 200 $^\circ\text{C}$ with a heating rate of 10 $^\circ\text{C}/\text{min}$ (stage I) and held there for 10 min to completely eliminate any possible crystallinity or residual stresses in the sample (stage II). Then samples were quenched to a desired isothermal crystallization temperature (stage III) and held there for 45 min to allow crystallization from the quiescent melt (stage IV). The temperature was ramped back up to 200 $^\circ\text{C}$ with a heating rate of 10 $^\circ\text{C}/\text{min}$ to probe the melting point after crystallization (stage V).

3.3. Optical Microscopy. Optical microscopy (OM) studies were carried out with a Nikon Microphot-SA microscope in conjunction with a Mettler hot stage (FP-82). Samples were prepared by cutting small pieces from prepared films. Samples weighing ~5 mg were melted on glass slides with coverslips to form thin films ~20–50 μm thick. The specimens were heated to 200 $^\circ\text{C}$ on a hot plate and held at that temperature for 5 min and then quickly inserted into a hot stage set at a prefixed crystallization temperature. The hot stage was calibrated with a melting point standard to ± 0.2 $^\circ\text{C}$ accuracy. The growth of spherulites was recorded on a VCR, and the growth rate data were measured from time-lapsed frames of spherulitic fronts. Polarized light and Hoffman modulation contrast

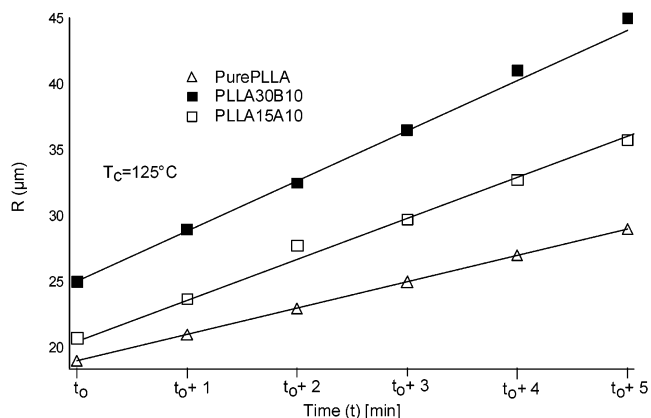


Figure 3. Radius of the growing spherulites as a function of time at 125 $^\circ\text{C}$ for neat PLLA, PLLA30B10, and PLLA15A10. The lines are fitted to the experimental data to calculate the slope and growth rate (G). t_0 denotes an arbitrary time after quenching to T_c when spherulites begin to grow and are observable in POM.

optics were utilized in order to observe the morphology. In addition, photographs were taken by a digital camera.

3.4. Scanning Electron Microscopy (SEM/EDS). A Hitachi S-4700 and JEOL 7400 field emission scanning electron microscope both equipped with an Oxford EDS (energy-dispersive X-ray spectroscopy) system were utilized to capture high-resolution images of spherulites and get an elemental map of the atomic elements present. To reduce electron beam damage, the samples were lightly carbon coated with a Denton carbon coater prior to imaging and EDS analysis.

4. Results and Discussion

4.1. Radial Growth Rate. The radial spherulite growth rates of neat PLLA and PLLA/organoclay nanocomposites were measured over time. Figure 3 shows representative data concerning the change in spherulite radius as a function of time at 125 $^\circ\text{C}$. In all samples the spherulite diameters increased linearly with time at all crystallization temperatures, indicating that growth rate was independent of the size of the spherulites. If noncrystallizable species are excluded from growing spherulites, they will build up on the crystallization growth front and consequently hinder the transport of crystallizable species from the melt to the growing edge.⁴² This phenomenon will give rise to a deviation from linear spherulite growth after the spherulite reaches a certain diameter. Since no such deviation from linearity in spherulite growth was observed in the nanocomposites (Figure 3), it can be concluded that the clay platelets are not excluded during spherulite growth. Additional evidence of clay incorporation in the crystalline regions is described in the EDS results (vide infra).

Measurements of spherulite radius (R) vs time (t) were performed on more than five different spherulites per experiment, and the growth rate ($G = dR/dt$) was calculated as the slope of the line fitted to the experimental data at a given crystallization temperature. Figure 4 shows the average growth rate at different crystallization temperatures. For the sake of brevity, only the results of neat PLLA and the nanocomposites with 10 wt % clay loadings are shown. Because of very slow crystallization kinetics and need of using other techniques such as self-seeding, crystallization temperatures above 145 $^\circ\text{C}$ are not examined in this work. In addition, because of very high nucleation densities, growth rate measurements at temperatures below 115 $^\circ\text{C}$ were not possible. Figure 4 shows that the growth rate increases

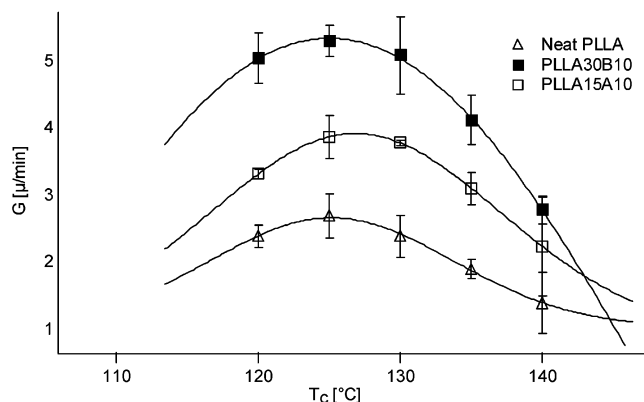


Figure 4. Spherulite growth rate (G) as a function of crystallization temperature (T_c) for neat PLLA, PLLA30B10, and PLLA15A10.

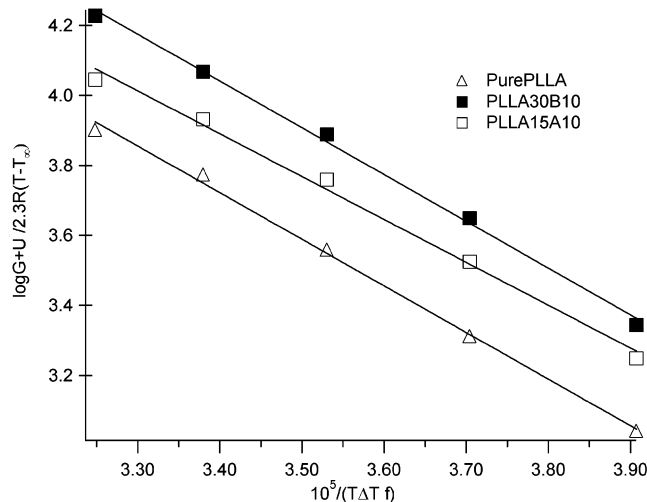


Figure 5. Secondary nucleation plots of linear growth rates, based on the values in Table 3, for neat PLLA, PLLA30B10, and PLLA15A10. (Uncertainties being below $\pm 2\%$ are not plotted for the sake of clarity.)

Table 2. Characteristics of Samples Prepared (Designation, Clay Type, and Clay Content)

| sample | type of clay | clay content (inorganic part), wt % |
|-----------|--------------|-------------------------------------|
| PLLA15A10 | Cloisite 15A | 10 |
| PLLA15A15 | Cloisite 15A | 15 |
| PLLA30B10 | Cloisite 30B | 10 |
| PLLA30B15 | Cloisite 30B | 15 |

by increasing crystallization temperature up to about 125 °C, and then it starts to decrease by further increasing the crystallization temperature. This behavior is well documented in the polymer crystallization literature.³⁵ The spherulite growth rate of PLLA30B10 is almost 2-fold that of neat PLLA. The data in Figure 4 can be analyzed using the growth rate expression (i). The values in Table 3 were used as input parameters. After some data treatment, Figure 5 can be obtained on the basis of the data points in Figure 4, and K_g and G_0 can be calculated with respect to the slope and intercepts of the fitted lines. These values are shown in Table 4. The K_g value for neat PLLA is almost identical with PLLA30B10 and is slightly larger than that of PLLA15A10. In addition, G_0 increases in the order of PLLA15A10 to neat PLLA and PLLA30B10 with PLLA30B10 exhibiting a G_0 of 2 times higher than neat PLLA and 3 times that of PLLA15A10.

Table 3. Parameters Used in Secondary Crystallization Calculations

| quantity | value | reference |
|--------------|--|-----------|
| U^* | 1500 cal mol ⁻¹ | 43 |
| T_m^0 | 480 K | 47 |
| T_g | 330 K | <i>a</i> |
| ΔH_f | 111.083×10^6 J m ⁻³ | 48 |
| σ_e | 60.89×10^{-3} J m ⁻² | 47 |
| <i>b</i> | 5.17×10^{-10} m | 47 |

^a Measured by DSC.

Table 4

| sample | G_0 [(μ m/min)] $\times 10^8$ | $K_g \times 10^{-5}$ | σ [J m ⁻²] $\times 10^{-3}$ |
|-----------|--------------------------------------|----------------------|--|
| pure PLLA | 1.79 ± 0.62 | 3.07 ± 0.05 | 15.57 ± 0.36 |
| PLLA30B10 | 3.87 ± 0.60 | 3.08 ± 0.06 | 15.62 ± 0.43 |
| PLLA15A10 | 1.14 ± 0.51 | 2.82 ± 0.03 | 14.30 ± 0.21 |

In the temperature range that the radial growth rate experiments were performed, neat PLLA crystallizes in regime II, $n = 2$.⁴³ In this regime the secondary nucleation rate is high, and multinucleation occurs on a layer before its completion. Since there is no significant change in the slope of the curves, K_g , in Figure 5, it can be concluded that the nanocomposites also crystallize in the same regime, and therefore, no regime change is observed.

The values of lateral surface energy, σ , can be calculated from K_g values (Table 4). It can be concluded that Cloisite 30B is not an effective nucleation agent compared to Cloisite 15A. This can be attributed to the compatibility/miscibility of the 30B clay organic modifier with the PLLA, resulting in lateral surface energies closer to that of neat PLLA while the lateral surface energy of the 15A system is lower. This argument is in good agreement with microscopy results (Figure 16, vide infra), showing much smaller spherulites and higher nucleation density in 15A vs 30B.

A significantly higher spherulite growth rate in PLLA30B suggests that fully dispersed clay platelets with similar surface energy to that of the neat polymer act as a template for spherulite growth, resulting in much larger spherulites. This is in contrast with PLLA15A where a low degree of matrix miscibility, and thus low dispersion, produces spherulite growth rates close to the bulk (in addition to a much higher nucleation rate, vide infra). We will see below that despite acting as a spherulite template, the overall extent of crystallinity in the dispersed PLLA30B system is much lower than in neat PLLA and PLLA15A. Therefore, while significantly templating spherulite superstructure, the dispersed PLLA30B organoclay is hindering the local extent of crystallization and, thus, the ultimate extent of bulk crystallinity. The exact mechanism of the proposed superstructure templating effect by the miscible organoclay is currently under further investigation.

4.2. Bulk Crystallization Kinetics. Figure 6 shows representative Avrami integral curves for neat PLLA, which are obtained on the basis of experimental crystallization isotherms probed by DSC (Figure 7). The crystallization half-time, $t_{1/2}$, the time that is required to reach 50% of total crystallinity, and induction time, the time after which crystallization can be detected by the DSC apparatus, are deduced from the Avrami integral curves and are shown in Figures 8 and 9. Based on Figure 8 induction time increases with the addition of Cloisite 30B compared to neat PLLA, while it decreases with the addition of Cloisite 15A. This implies that due to high interfacial energy differences between

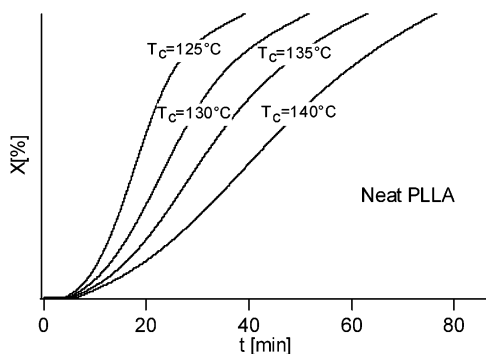


Figure 6. Integral crystallization curves (conversion vs time) for neat PLLA obtained at different crystallization temperatures.

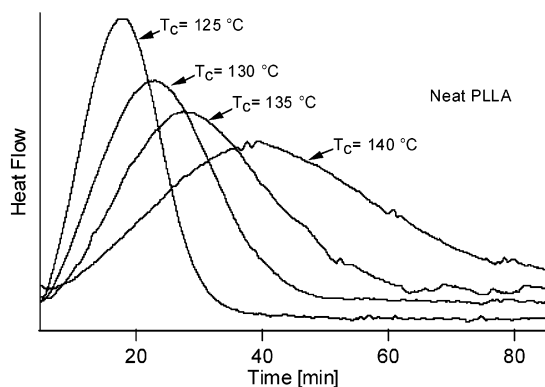


Figure 7. Crystallization isotherms of neat PLLA at different crystallization temperatures.

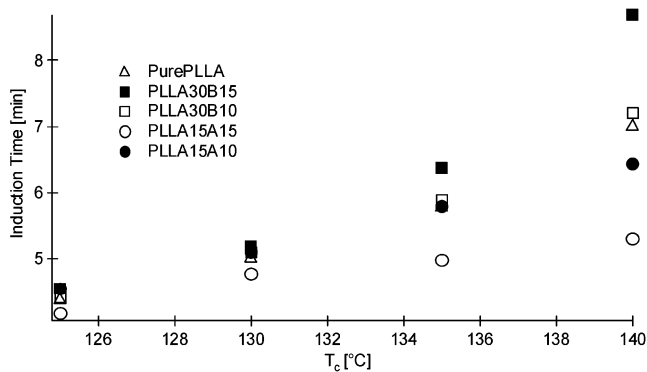


Figure 8. Induction time vs crystallization temperature. Induction time increases with the addition of Cloisite30B filler from 10 to 15 wt % while it decreases with the addition of Cloisite 15A from 10 to 15 wt %.

PLLA and the modifier used in Cloisite 15A, less time is needed for PLLA spherulites to heterogeneously nucleate so Cloisite 15A acts as a nucleating agent while Cloisite 30B does not. Moreover, Figure 9 indicates that the bulk crystallization half-time in the case of PLLA15A15 is significantly smaller than neat PLLA and PLLA30B15, implying that faster overall bulk kinetics due to increased spherulite nucleation are achieved in the intercalated case. This phenomenon is seen in most of the cases in which nucleating species with high interfacial energies are added to the polymer matrix.^{21,29,30,32,44} On the other hand, on the basis of Figure 9, Cloisite 30B has retarded the overall crystallization of PLLA which can be attributed to the high degree of miscibility between the modifier and the matrix. Thus, the dispersed clay platelets hinder the

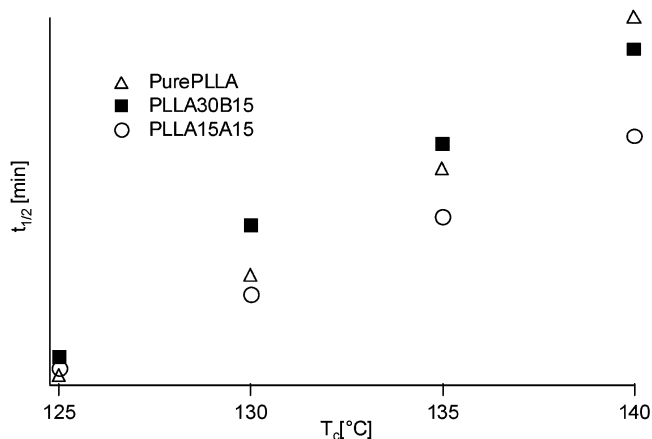


Figure 9. Average half-time of crystallization, $t_{1/2}$, vs crystallization temperature. In PLLA30B15, crystallization kinetics decrease while in PLLA15A15 crystallization kinetics increase.

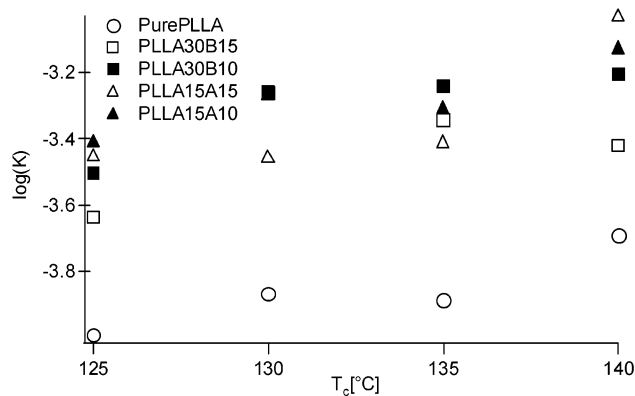
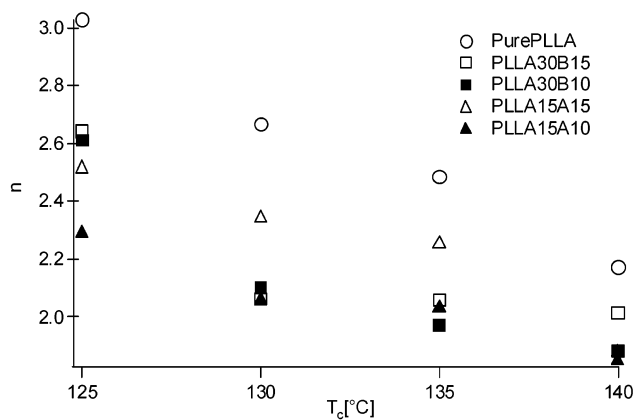


Figure 10. Avrami parameters vs crystallization temperature for different samples.

chain-folding mechanism needed for local PLLA crystallization. Somewhat similar results were obtained by Fornes et al.²⁷ where it was shown that high clay loadings can retard overall bulk crystallization kinetics.

On the basis of expression iv Avrami parameters were calculated (Figure 10). The Avrami exponent, n , represents the dimensionality of the growth, which decreases in all of the samples by increasing crystallization temperature. The n values in this temperature range are between 2 and 3, signifying a spherulitic morphology (Figure 10). In ideal cases $n = 3$ which indicates spherical growth while $n = 2$ indicates circular disk shape growth.³⁵ Therefore, the observed n values from all samples suggest that well-defined spherulitic structures can be obtained at higher undercoolings. As shown

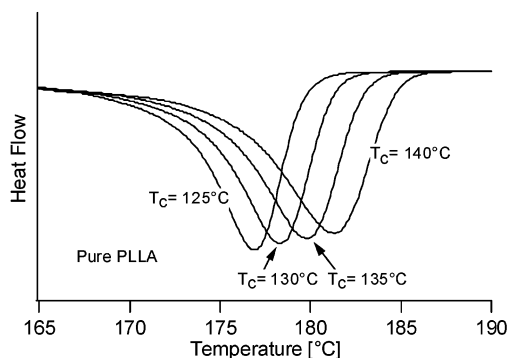


Figure 11. Endothermic peaks of neat PLLA samples crystallized at different temperatures. The melting point, or temperature at which the endothermic maximum is observed, increases by crystallizing at higher temperatures.

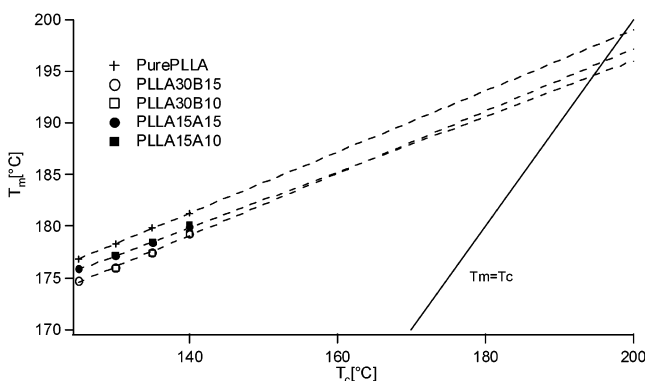


Figure 12. Crystallinity melting point, T_m , as a function of the crystallization temperature, obtained from DSC measurements. The extrapolation of the lines fitted to the experimental data to $T_m = T_c$ are shown as dashed lines.

in Figure 10, by the addition of clay, the growth geometry is more 2-dimensional (disk shaped) rather than spherical growth. Moreover, in each of the samples the $\log(K)$ term slightly increases by increasing crystallization temperature, having the lowest values in the case of neat PLLA.

4.3. Crystallinity. A representative graph showing the endotherm peak shift to higher temperatures at lower undercoolings for pure PLLA is shown in Figure 11. On the basis of the curves shown in Figure 11 for different samples, Figure 12 can be obtained. Melting points in the case of nanocomposites are relatively lower than neat PLLA, suggesting thinner lamella crystals or defective crystalline regions present in the nanocomposites.

Figure 12 shows that melting point of neat PLLA and the nanocomposites increases by increasing the isothermal crystallization temperature (T_c), indicating that the perfection and thickness of the growing PLLA lamella crystals increase at higher T_c 's, as expected. By fitting these data points to a straight line and extrapolating it to $T_m = T_c$, the equilibrium melting temperature, T_m^* , can be estimated.^{45,46} This value is required for super cooling calculations. The T_m^* values for neat PLLA and the nanocomposites are very similar within the experimental errors. The $T_m^* = 471$ K value obtained here for neat PLLA conflicts with Kalb et al.'s⁴⁷ value of 488 K or Vasanthakumari and co-worker's⁴³ value of 480 K. This might be due to the differences in degree of stereoregularity of the samples or because of the fact that in this work T_m^* is obtained based on higher undercooling empirical data. Throughout this contribu-

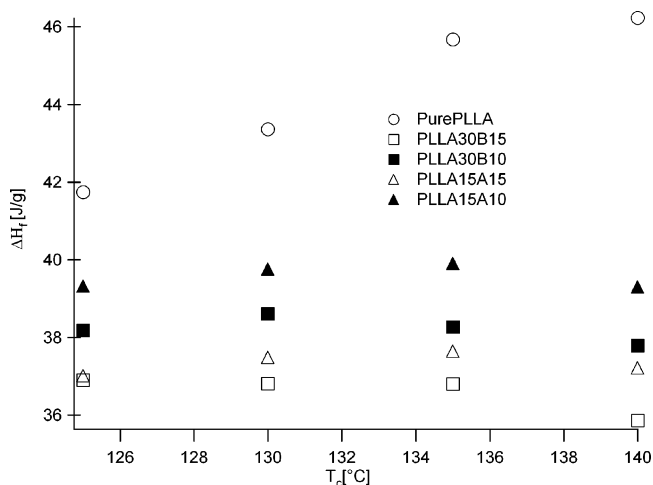


Figure 13. Heat of fusion as a function of crystallization temperature.

tion $T_m^* = 480$ K, the median value of the literature values and those determined herein, is applied in the calculations.

The heat of fusion as determined by area under the melting peaks (Figure 11) was calculated by integration of melting exotherms. Heat of fusion is directly proportional to the crystallinity of the sample, and the degree of crystallinity, x_c , can be calculated by

$$x_c = \frac{\Delta H_f}{(1 - \phi)\Delta H_f^*} \times 100\%$$

where ϕ is the weight fraction of the filler in nanocomposite, ΔH_f is the heat of fusion, and ΔH_f^* denotes heat of fusion for an infinitely large crystal. ΔH_f^* of PLLA was measured by Fischer et al.,⁴⁸ and it was reported to be in the range of 81.3–93.0 J/g.

The heat of fusion is shown as a function of crystallization temperature for different nanocomposites and the neat PLLA (Figure 13). In the case of neat PLLA, crystallinity increases by increasing the crystallization temperature while in the case of nanocomposites it remains almost unchanged at a much less degree of crystallinity. Moreover, at the same clay loadings PLLA30B nanocomposites have much less crystallinity compared to that of PLLA15A system. This phenomenon was also seen in the samples directly crystallized from solution.³⁴ It can be concluded that higher extent of exfoliation, PLLA30B, has the highest effect in lowering the crystallinity of this hybrid systems.

In summary, the high degree of miscibility between organic modifier used in Cloisite 30B and the polymer matrix decreases the bulk crystallization rate and increases the induction time by both limiting local crystallization and limiting nucleation. Overall, a low degree of crystallinity was observed in PLLA30B relative to the neat PLLA matrix and intercalated PLLA15A nanocomposites, which can be attributed to the high clay dispersions observed in PLLA30B system.

4.4. Microscopy. A scanning electron microscopy image of PLLA30B10 after melting at 200 °C and crystallization at 120 °C is shown in Figure 14a. The boundary between any two adjacent spherulites is straight, which indicates that the spherulites growth rates are equal. No sheaflike structure can be recognized on the surface of the spherulites, which is in agreement

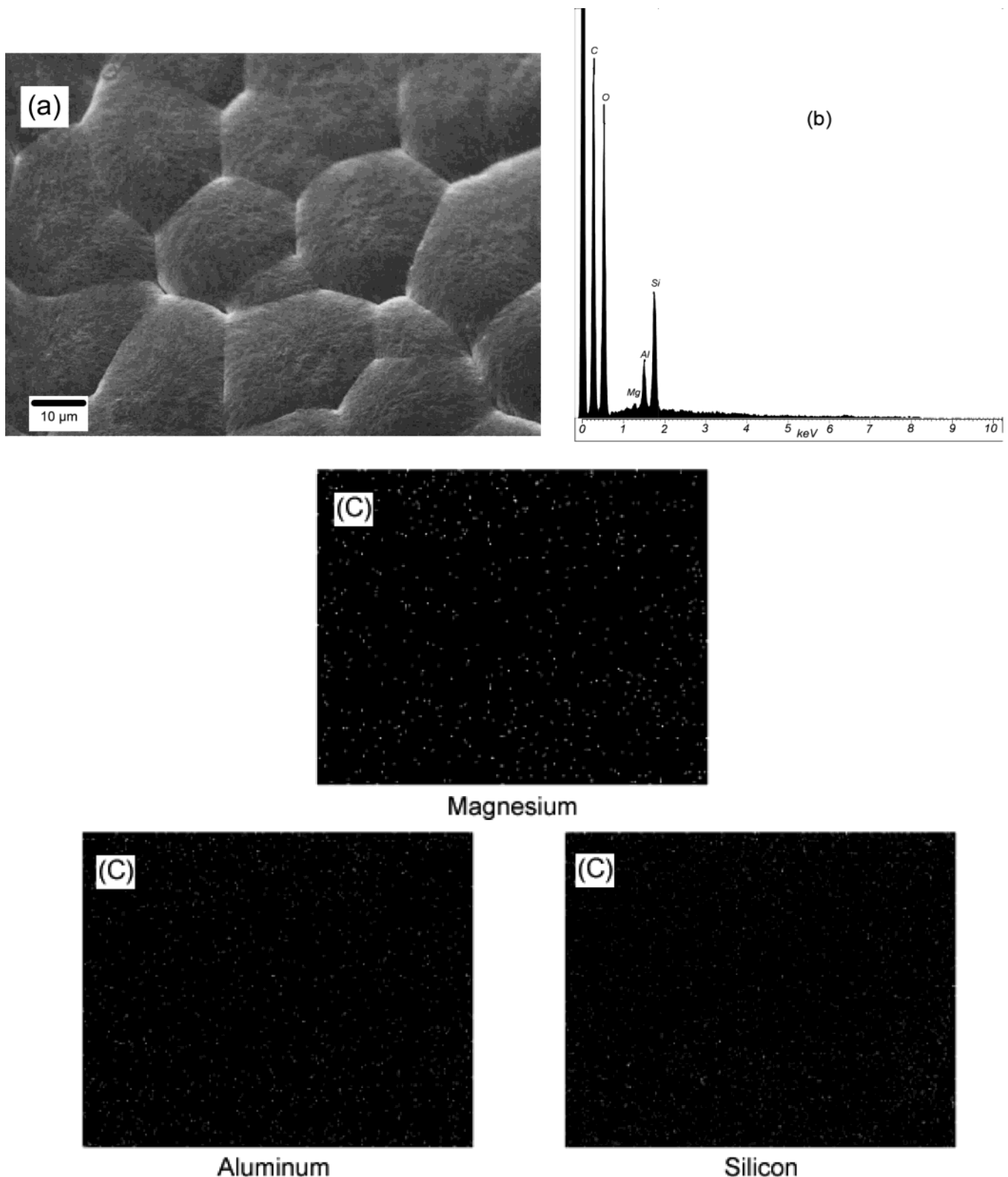


Figure 14. (a) SEM micrograph of PLLA30B10 melted at 200 °C and crystallized at 120 °C. (b) Elemental analysis of the same area in (a). (c) EDS compositional mapping of (a) highlighting magnesium, aluminum, and silicon elements, the constituents of montmorillonite type clay.

with optical light microscopy and AFM experiments (Figure 16c,d).

The chemical structure of montmorillonite clay is $M_x(\text{Al}_{4-x}\text{Mg}_x)\text{Si}_8\text{O}_{20}(\text{OH})_4$, where M is a monovalent cation and x is the degree of isomorphous substitution.¹ In the case of organically modified clay, a portion or all of the M is exchanged with the organic

modifier. Because of its size (lateral dimension of ca. 1 μm and thickness of ca. 1 nm) clay platelets cannot be incorporated within the crystal structure of PLLA and should be excluded from the growing crystalline phase, thus trapped in amorphous regions of the spherulites or segregated on the spherulite boundaries. However, the independence of spherulite growth

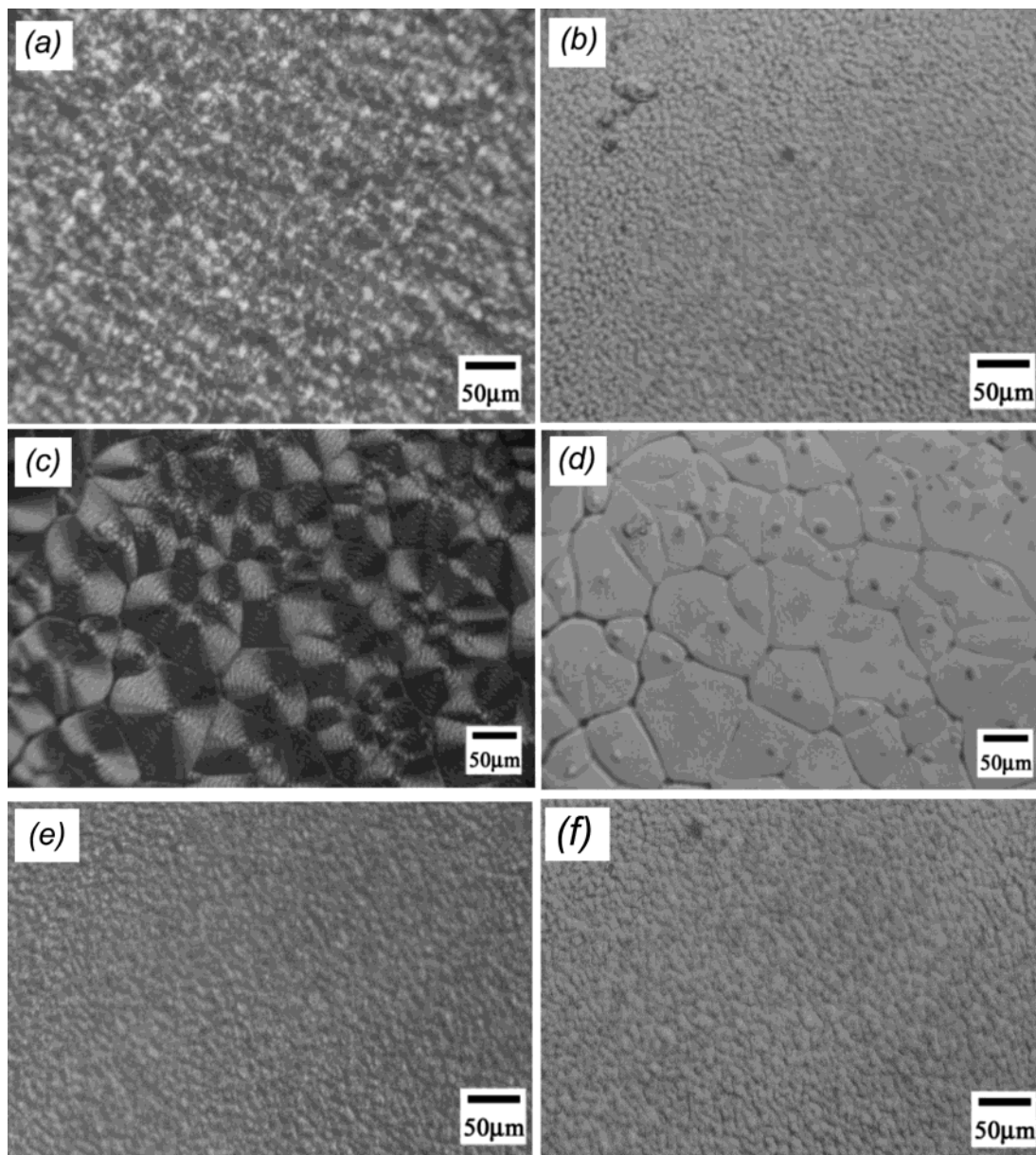


Figure 15. Polarized optical microscopy (a, c, e) and bright field (b, d, f) images of solution-cast films of neat PLLA (a, b), PLLA30B10 (c, d), and PLLA15A10 (e, f).

rates on clay loading described earlier strongly suggests the encapsulation of clay throughout the semi-crystalline spherulite. To further study the final state of clay in the crystalline material, energy dispersive spectroscopy (EDS) was performed on recrystallized nanocomposite samples. EDS measures the X-rays emitted during electron bombardment of a particular sample area in SEM and determines its chemical composition. By rastering the electron beam over an area of interest, an X-ray map, showing spatial variation of elements in the sample, can be obtained. In this work we have mapped the surface of the films with respect to silicate layer constituent elements—Al, Mg, and Si—and observed the spatial arrangement of the silicate layers. Figure 14b shows the elements present in the area shown in Figure 14a, and Figure 14c shows an X-ray map of these elements in the same area. On the basis of Figure 14c it can be said that silicate layers are randomly distributed within the polymer matrix and are not excluded from growing

spherulites, causing agglomeration at the spherulite boundaries.

Polarized light and bright field optical micrographs of as-cast neat PLLA and PLLA30B10 are shown in Figure 15. The spherulite sizes in the Cloisite 30B reinforced composite are significantly larger than that observed in the neat polymer. This can be attributed to the fact that Cloisite 30B does not act as a nucleating agent and increases the spherulite growth rate. Moreover, the concentric bands present in the PLLA30B10 spherulites denote presence of a high degree of lamellar crystal twisting.³⁵

Optical light micrographs with a quarter wave plate and AFM images of neat PLLA and PLLA30B10 crystallized at 120 °C from the quiescent melt are shown in Figure 16. Like as-cast samples (Figure 15), larger spherulites are present in the case of PLLA30B10 compared to neat PLLA. The AFM image (Figure 16b) shows the existence of sheaflike structure in neat PLLA while, despite the fact that PLLA30B10 also crystallized

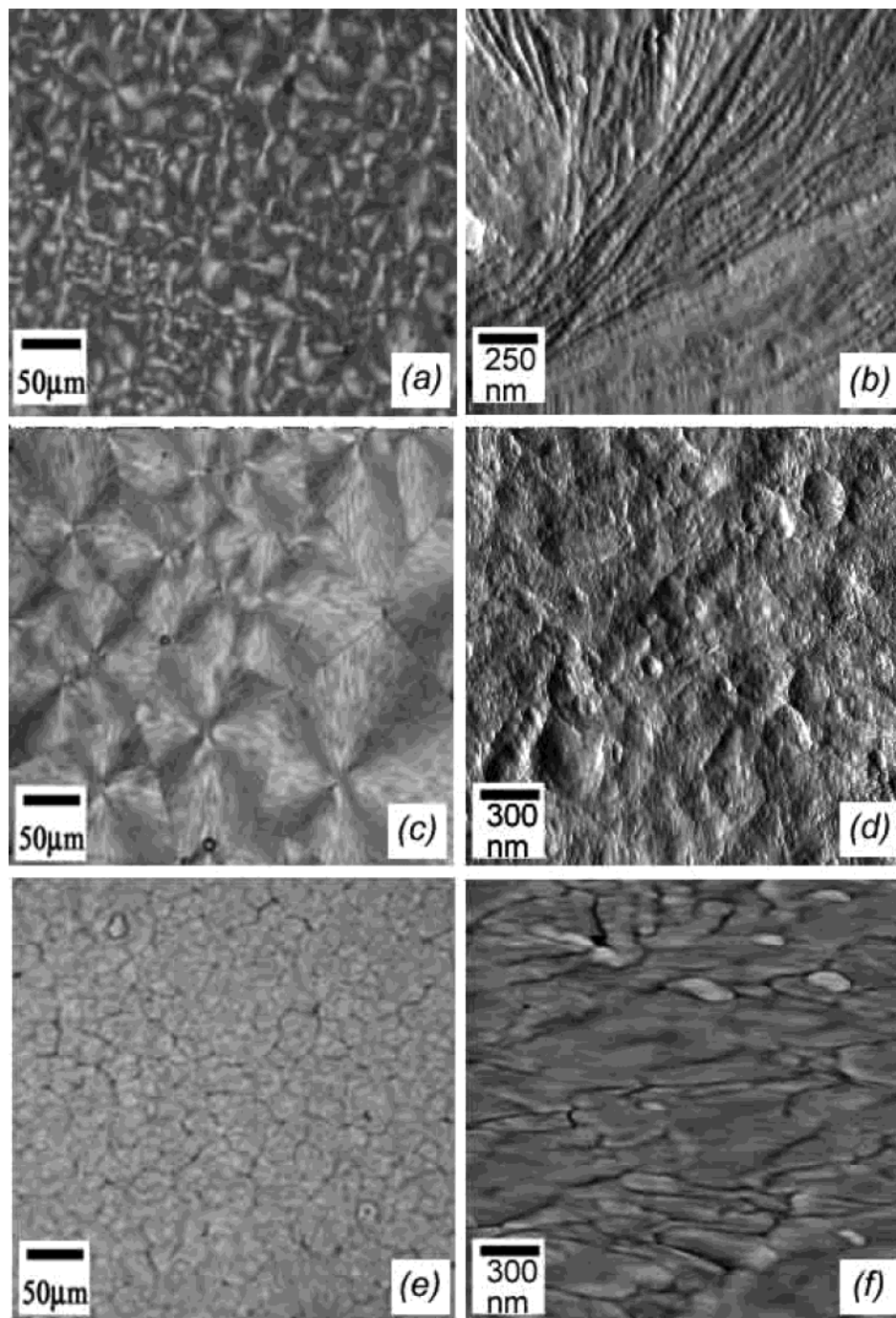


Figure 16. Polarized optical microscopy (a, c, e) and AFM amplitude (b, d, f) images of neat PLLA (a, b), PLLA30B10 (c, d), and PLLA15A10 (e, f) crystallized from quiescent melt at 120 °C.

in the form of spherulites, there is no sheaflike structure present (Figure 16d). This is further evidence that dispersed clay locally disrupts the chain folding polymer crystallization while templating the long scale spherulitic superstructure.

5. Conclusion

Using optical microscopy, scanning electron microscopy, and differential scanning calorimetry techniques, we have studied the effects of organically modified clay addition on the isothermal crystallization behavior of PLLA. Similar to previous observations of different polymers, the clay sheets significantly altered the crystallization properties of PLLA but in ways unexpected from conventional filled polymer systems. More-

over, the degree of clay miscibility with the matrix and thus clay dispersion in the PLLA matrix defines the crystallization and final morphology of nanocomposites crystallized both from solution and the melt. When the clay organic modifier is highly miscible with PLLA (exfoliated nanocomposite case), spherulite nucleation is low. The bulk crystallization rate is slower, and the extent of crystallinity is much lower than that of neat PLLA. Conversely, spherulite radial growth rate is significantly higher compared to that of neat polymer. This might be due to a superstructure templating effect associated with fully exfoliated clay platelets that, in turn, hinders local lamellar crystallization and leads to the least degree of crystallinity observed. Low spherulite nucleation behavior coupled with higher radial growth

rate resulted in much greater final spherulite sizes. In contrast, in nanocomposites with an intercalated morphology due to lower miscibility between the polymer matrix and the organic modifier, the clay acts as an effective nucleating agent leading to increased bulk crystallization rates, resulting in much finer spherulites and a higher overall degree of crystallinity as compared to the exfoliated case.

During isothermal crystallization from quiescent melt, clay platelets were not excluded from growing spherulites but were trapped within the spherulites. This conclusion is also based on the fact that linear spherulite growth rates were observed regardless of the spherulite size, and elemental mapping of the crystallized samples did not show any segregation of the clay platelets in the spherulite boundary regions.

Avrami analysis indicates that clay incorporation, regardless of the modifier used, drove the system toward a two-dimensional growth geometry while three-dimensional spherical growth was observed in neat polymer. AFM revealed no sheaflike structure in the fully exfoliated nanocomposites. The low degree of crystallinity with addition of miscible clay suggests that clay disrupts the local chain folding and lamellae formation in the matrix. This phenomenon was observed in samples crystallized from both solution and the quiescent melt. Moreover, at the same crystallization conditions the exfoliated nanocomposite system exhibited lowest melting points compared to neat PLLA, suggesting smaller crystalline domains and less crystal perfection.

More investigations are necessary in order to fully elucidate the effect of incorporating modified/unmodified high surface area inorganic phases on both bulk crystallization and spherulitic growth rate of the macromolecules. The initial results presented herein suggest that one can engineer the final barrier and mechanical properties of nanocomposite materials by incorporating a mixture of miscible and immiscible organoclays, thereby controllably tuning degree of crystallinity, final spherulitic morphology, and degree of dispersion of clay throughout the matrix. By using exclusively miscible organoclay reinforcement, one sacrifices crystallinity while gaining dispersion.

Acknowledgment. We acknowledge the support of this work by the National Science Foundation Career Award DMR-0348147. The authors are grateful to Prof. Jerold M. Schultz for his stimulating discussions and helpful ideas throughout this work and to Florian Linse for his assistance in some of optical microscopy experiments. The authors also thank the Center of Composite Materials (CCM) at UD for use of DMA, Dr. Chaoying Ni at the College of Engineering Keck electron microscopy laboratory, and Dr. Kirk Czymmek and Deborah Powell at the Delaware Biotechnology Institute (DBI).

Supporting Information Available: Figures showing crystallization isotherms and endothermic peaks of PLLA, PLLA30B10, and PLLA15A10. This material is available free of charge via the Internet at <http://pubs.acs.org>.

References and Notes

- Alexandre, M.; Dubois, P. *Mater. Sci. Eng., R* **2000**, *28*, 1–63.
- Kojima, Y.; Usuki, A.; Kawasumi, M.; Okada, A.; Kurauchi, T.; Kamigaito, O. *J. Polym. Sci., Part A: Polym. Chem.* **1993**, *31*, 983–986.
- Fukushima, Y.; Inagaki, S. *J. Inclusion Phenom.* **1987**, *5*, 473–482.
- Messersmith, P. B.; Giannelis, E. P. *J. Polym. Sci., Part A: Polym. Chem.* **1995**, *33*, 1047–1057.
- Gilman, J. W.; Jackson, C. L.; Morgan, A. B.; Harris, R.; Manias, E.; Giannelis, E. P.; Wuthenow, M.; Hilton, D.; Phillips, S. H. *Chem. Mater.* **2000**, *12*, 1866–1873.
- Kojima, Y.; Usuki, A.; Kawasumi, M.; Okada, A.; Fukushima, Y.; Kurauchi, T.; Kamigaito, O. *J. Mater. Res.* **1993**, *8*, 1185–1189.
- Mucha, M.; Marszalek, J.; Fidrych, A. *Polymer* **2000**, *41*, 4137–4142.
- Liang, J. Z.; Li, R. K. Y.; Tjong, S. C. *J. Appl. Polym. Sci.* **1999**, *71*, 687–692.
- Faulkner, D. L.; Schmidt, L. R. *Polym. Eng. Sci.* **1977**, *17*, 657–665.
- Bassett, D. C. *Principles of Polymer Morphology*; Cambridge University Press: Cambridge, 1981.
- Kennedy, M.; Turturro, G.; Brown, G. R.; StPierre, L. E. *Nature (London)* **1980**, *287*, 316–317.
- Kennedy, M. A.; Brown, G. R.; StPierre, L. E. *Polym. Compos.* **1984**, *5*, 307–311.
- Kennedy, M. A.; Brown, G. R.; StPierre, L. E. *Polym. Eng. Sci.* **1990**, *30*, 769–775.
- Kennedy, M. A.; Turturro, G.; Brown, G. R.; StPierre, L. E. *J. Polym. Sci., Part B: Polym. Phys.* **1983**, *21*, 1403–1413.
- Burke, M.; Young, R. J.; Stanford, J. L. *Polym. Bull. (Berlin)* **1993**, *30*, 361–368.
- Raimo, M.; Martuscelli, E. *J. Appl. Polym. Sci.* **2003**, *90*, 3409–3416.
- Wang, K.; Wu, J. S.; Zeng, H. M. *Eur. Polym. J.* **2003**, *39*, 1647–1652.
- Thomason, J. L.; Vanrooyen, A. A. *J. Mater. Sci.* **1992**, *27*, 889–896.
- Wang, C.; Hwang, L. M. *J. Polym. Sci., Part B: Polym. Phys.* **1996**, *34*, 47–56.
- Murthy, N. S.; Aharoni, S. M.; Szollosi, A. B. *J. Polym. Sci., Part B: Polym. Phys.* **1985**, *23*, 2549–2565.
- Tseng, C. R.; Lee, H. Y.; Chang, F. C. *J. Polym. Sci., Part B: Polym. Phys.* **2001**, *39*, 2097–2107.
- Tseng, C. R.; Wu, J. Y.; Lee, H. Y.; Chang, F. C. *Polymer* **2001**, *42*, 10063–10070.
- Tseng, C. R.; Wu, S. C.; Wu, J. J.; Chang, F. C. *J. Appl. Polym. Sci.* **2002**, *86*, 2492–2501.
- Vanderhart, D. L.; Asano, A.; Gilman, J. W. *Chem. Mater.* **2001**, *13*, 3796–3809.
- VanderHart, D. L.; Asano, A.; Gilman, J. W. *Chem. Mater.* **2001**, *13*, 3781–3795.
- Lincoln, D. M.; Vaia, R. A.; Wang, Z. G.; Hsiao, B. S.; Krishnamoorti, R. *Polymer* **2001**, *42*, 9975–9985.
- Fornes, T. D.; Paul, D. R. *Polymer* **2003**, *44*, 3945–3961.
- Maiti, P.; Nam, P. H.; Okamoto, M.; Hasegawa, N.; Usuki, A. *Macromolecules* **2002**, *35*, 2042–2049.
- Somwangthanaroj, A.; Lee, E. C.; Solomon, M. J. *Macromolecules* **2003**, *36*, 2333–2342.
- Strawhecker, K. E.; Manias, E. *Chem. Mater.* **2003**, *15*, 844–849.
- Nam, J. Y.; Ray, S. S.; Okamoto, M. *Macromolecules* **2003**, *36*, 7126–7131.
- Hambir, S.; Bulakh, N.; Kodgire, P.; Kalgaonkar, R.; Jog, J. P. *J. Polym. Sci., Part B: Polym. Phys.* **2001**, *39*, 446–450.
- Maiti, P.; Okamoto, M. *Macromol. Mater. Eng.* **2003**, *288*, 440–445.
- Krikorian, V.; Pochan, D. J. *Chem. Mater.* **2003**, *15*, 4317–4324.
- Schultz, J. M. *Polymer Crystallization: The Development of Crystalline Order in Thermoplastic Polymers*; Oxford University Press: New York, 2001.
- Hoffman, J. D. *Polymer* **1982**, *23*, 656–670.
- Hoffman, J. D. *Polymer* **1983**, *24*, 3–26.
- Hoffman, J. D.; Weeks, J. J. *J. Res. Natl. Bur. Stand., Sect. A: Phys. Chem.* **1962**, *66*, 13.
- Avrami, M. *J. Chem. Phys.* **1941**, *9*, 177.
- Avrami, M. *J. Chem. Phys.* **1940**, *8*, 212.
- Avrami, M. *J. Chem. Phys.* **1939**, *7*, 1103.
- Schultz, J. M. *Polymer* **1991**, *32*, 3268–3283.
- Vasanthakumari, R.; Pennings, A. J. *Polymer* **1983**, *24*, 175–178.
- Wu, H. D.; Tseng, C. R.; Chang, F. C. *Macromolecules* **2001**, *34*, 2992–2999.

- (45) Roitman, D. B.; Marand, H.; Miller, R. L.; Hoffman, J. D. *J. Phys. Chem.* **1989**, *93*, 6919–6926.
- (46) Hoffman, J. D.; Miller, R. L.; Marand, H.; Roitman, D. B. *Macromolecules* **1992**, *25*, 2221–2229.
- (47) Kalb, B.; Pennings, A. J. *Polymer* **1980**, *21*, 607–612.

- (48) Fischer, E. W.; Sterzel, H. J.; Wegner, G. *Kolloid Z. Z. Polym.* **1973**, *251*, 980–990.

MA049283W